[Electronic Supplementary Information]

Electronic interaction between dimethyl carbonate and Li^+ studied by attenuated total reflectance far-ultraviolet spectroscopy

Hitomi Sato, Nami Ueno* and Ichiro Tanabe*

SI 1. Differences between the experimental and simulated results

For both pure DMC and Li^+DMC, the experimentally observed peak wavelengths were longer than simulated ones. Two reasons mainly contribute to this difference.

Firstly, TD-DFT calculations were performed using only one molecule in the simulation model. However, in the experiments, there are numerous DMC and Li^+ present in the measurement space.

Secondly, as described in the main text, the ATR spectrum is different from the transmission spectrum. While the Kramers-Kronig Transformation (KKT) and the Fresnel formulas are commonly used to convert ATR spectra to transmission spectra, this process requires accurate optical constants of the prism and measured spectral data across the infinite frequency range. By applying some approximations such as Maclaurin's formula, the KKT is often used in infrared spectroscopy. Ikehata *et al.* applied the KKT to ATR-FUV spectra [Appl. Spectrosc., 2017, 71, 1530], experiencing numerous difficulties due to the inherent properties of some instrumental functions. In this study, the complex spectral variations dependent on Li^+ concentration present an even greater challenge for the application of KKT. As a result, the acquired ATR-FUV spectra were used without any transformation.

Consequently, there is a difference between the experimental and simulated spectra. However, as emphasized in the main text, the appearance of absorption in the FUV region and the redshift of the absorption wavelength upon the presence of Li^+ are well reproduced by TD-DFT calculations.

SI 2. Effect of the counter anion ($[BF_4]^-$) on the ATR spectrum

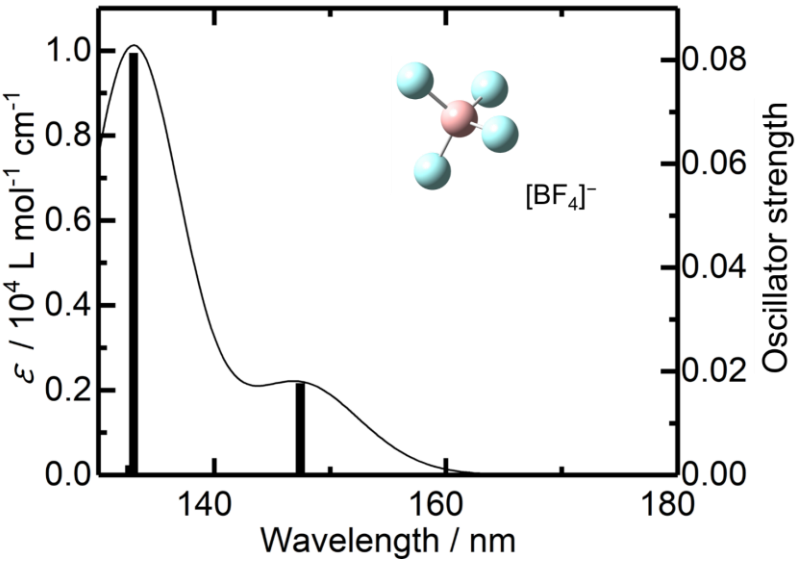

Figure S1 Time-dependent density functional theory (TD-DFT) calculated oscillator strengths and molar extinction coefficients (ε) of $[BF_4]^-$. This TD-DFT calculation was performed using the TD-CAM-B3LYP/aug-cc-pVTZ basis set. Based on the calculated vertical transition energies and oscillator intensities, the absorbance spectra were simulated assuming an energy width of 0.5 eV for each transition.

In the TD-DFT calculation of $[BF_4]^-$ (Figure S1), the oscillator strength and molar extinction coefficient (ε) are much smaller than DMC and Li^+DMC (Figure 2(a)). Additionally, the concentration of $Li[BF_4]$ is low (0.0-1.5 M). Therefore, it can be concluded that the effect of $[BF_4]^-$ is neglected in this study.

SI 3. Details of TD-DFT calculations for DMC and Li^+DMC

Table S1 Calculated transition wavelengths, oscillator strength, main initial states, and main final states of DMC.

Wavelength / nm	Oscillator strength	Initial state	Final state
145.4	0.0239	HOMO	LUMO+3
141.8	0.0312	HOMO-1	LUMO+2
140.1	0.1336	HOMO-1	LUMO+8
137.1	0.0096	HOMO-2	LUMO+3
134.1	0.0347	HOMO-2	LUMO+2
133.2	0.0544	HOMO-3	LUMO

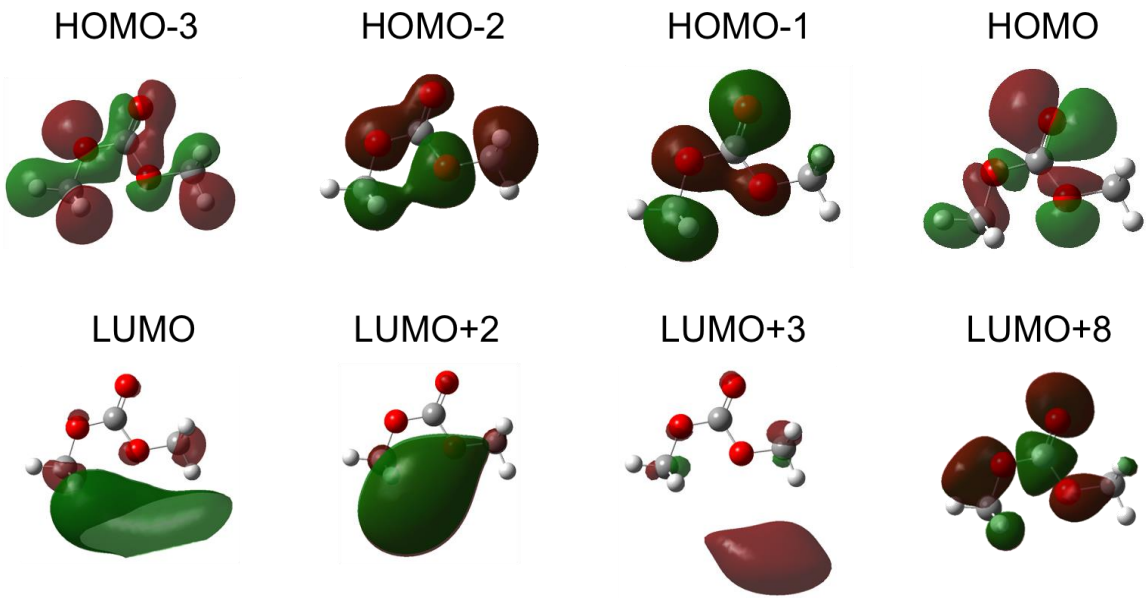

Figure S2 Visualized molecular orbitals of the orbitals listed in Table S1. All molecular orbitals were obtained under the same conditions, with the equivalent number set to 0.02.

Table S2 Calculated transition wavelengths, oscillator strength, main initial states, and main final states of Li^+DMC.

Wavelength / nm	Oscillator strength	Initial state	Final state
148.1	0.2331	HOMO-1	LUMO+1
142.8	0.1828	HOMO-1	LUMO+1
132.8	0.0144	HOMO-3	LUMO
130.8	0.0099	HOMO-1	LUMO+3

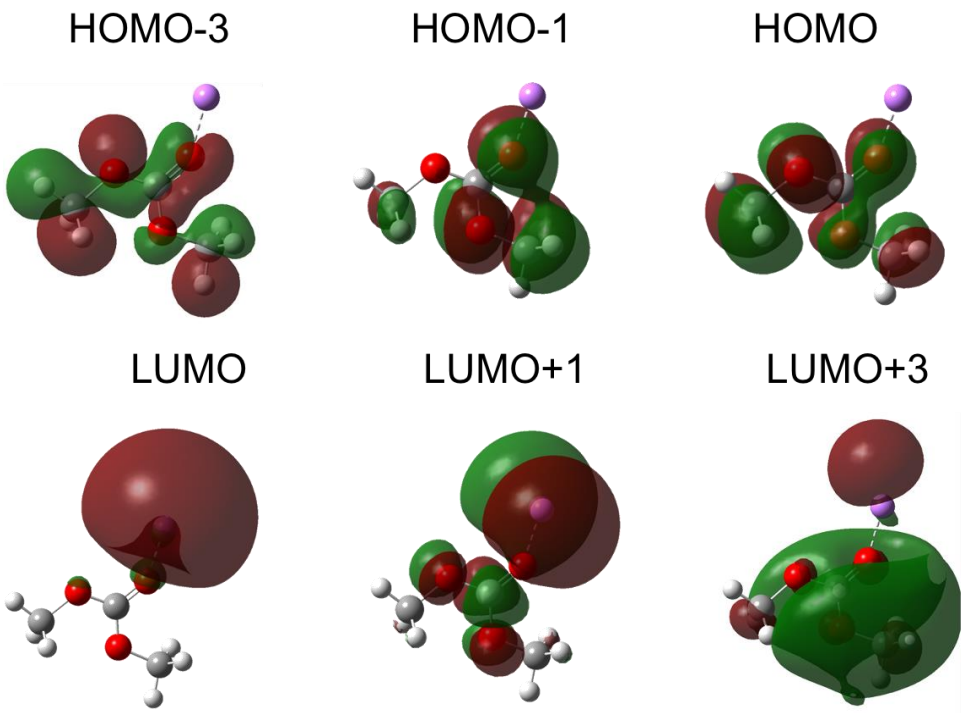

Figure S3 Visualized molecular orbitals of the orbitals listed in Table S2. All molecular orbitals were obtained under the same conditions, with the equivalent number set to 0.02.

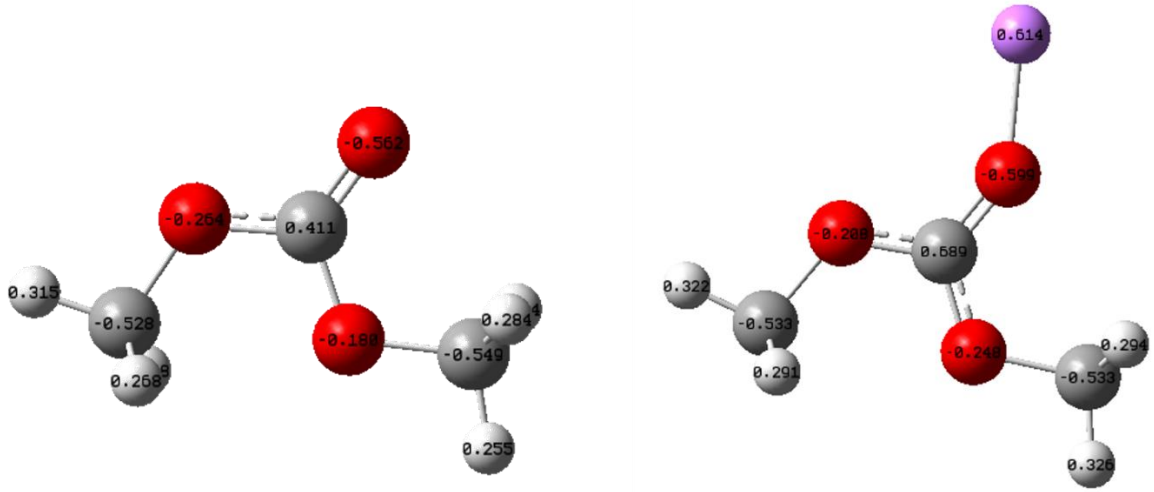

Figure S4 Calculated charge distributions of DMC and Li^+DMC

When comparing Figures S2 and S3, the most important point, as mentioned in the main text, is the electron distribution around Li^+ at the LUMO or LUMO+1 levels. Additionally, it's noted that the electron distribution of the HOMO or HOMO-1 levels is altered by the addition of Li^+. As shown in Figure S4, upon the addition of Li^+, the charge distribution within the DMC changed. In particular, the significant changes in the charge distributions over the three oxygen atoms have occurred due to the electron being drawn towards Li^+. The presented charge distribution of HOMO in DMC matches with the reported one.[S1] While DFT simulations regarding charge transfer between Li^+ and other solvents such as ethylene carbonate was published,[S2,S3] there is no report regarding the charge distribution of pure DMC coordinating to Li^+ to our knowledge. The interactions (i.e. electronic interactions and Van der Waals interactions) of DMC molecules coordinating to Li^+ were investigated using both quantum chemical calculations and molecular dynamics simulations.[S3] The research on such interactions involving solvation structures is currently under going.

References

S1 B. Deng, H. Wang, X. Li, Y. Ding, D. Sun, J. Ma, M. Chen, T. Chen, F. Gao, M. Qu and G. Peng, *Energy Technol.*, 2019, **7**, 1800981.

S2 D. Xiao, Q. Li, D. Luo, R. Gao, Z. Li, M. Feng, T. Or, L. Shui, G. Zhou, X. Wang and Z. Chen, *Adv. Funct. Mater.*, 2021, **31**, 2011109.

S3 M. Shakourian-Fard, G. Kamath and S. K. R. S. Sankaranarayanan, *ChemPhysChem*, 2016, **17**, 2916.

SI 4. Details of multivariate analysis

This section explains the Multivariate Curve Resolution-Alternating Least Squares (MCR-ALS) technique, employed to elucidate the origins of spectral change observed. As a brief explanation of MCR-ALS: it extracts the pure spectral and those of the contribution data from the data matrix utilizing a bilinear model and the profiles of pure components consisting two-way. The correlation between the data matrix and the profiles of pure components is calculated in the subsequent equation:

$$\boldsymbol{D}_{i,j} = \boldsymbol{S}_{n,j}^{T}\boldsymbol{C}_{i,n} + \boldsymbol{E}$$

wherein, i, j, and n denote the number of samples, variables, and components, respectively. Variables represent data points within the wavelength spectrum used for the MCR-ALS. The pure components profile refers to both spectral and concentration data in this study and represents the concentration profile $\boldsymbol{C}_{i,n}$ and the pure spectra $\boldsymbol{S}_{n,j}^{T}$. $\boldsymbol{C}_{i,n}$ denotes the variation in the Li-salt concentration of samples shown in Figure 1, whereas $\boldsymbol{S}_{n,j}^{T}$ will be elucidated later. The data matrix $\boldsymbol{D}_{i,j}$ is constituted the spectral data shown in Figure 1, with $\boldsymbol{E}$ signifying the error, but also inclusive of residuals due to any components potentially unaccounted for by the bilinear model. $\boldsymbol{E}$ is considered an error in this study. First, the determination of the total number of the component n was achieved through Singular Value Decomposition (SVD). SVD is based on Eigenvalue decomposition and its extension to the $m \times n$ matrix to generalization.

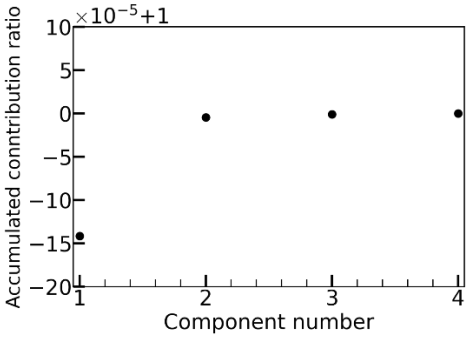

Figure S5 Accumulated contribution calculated by the result of SVD using the ATR-FUV spectra derived from DMC and Li[BF_4] DMC solutions plotted versus the component numbers.

Figure S5 the accumulated contribution derived from the singular value and is plotted versus the component number. Figure S5 indicates major part of the variation in the data matrix is caused by component 1 but significant variance between components 1 and 2. However, contributions due to component numbers over 2 can be ignored because the change is hardly found other than in components 1-2. This suggests that the spectral variations (data matrix) stem predominantly from two principal characters.

Subsequently, $\boldsymbol{S}_{n,j}^{T}$ are defined as three components derived from SVD outcomes: two fundamental components and an auxiliary noise component. The principal components include the experimentally measured spectrum of DMC and a spectrum generated via the Gaussian function (standard deviation: 10, amplitude: 1.0, peak center: 155.0 nm for $[BF_4]^-$ or 157.0 nm for $[TFSI]^-$), with the peak center determined experimentally. The noise component is randomly variable within 0 to 1, scaled by 10^{-5} in the ALC process. In this process, the spectral shape of DMC is maintained constant, indicating spectral variations are in component 2, barring those attributable to DMC concentration changes. Running the ALS process necessitates expanding the error threshold to accommodate alterations in the spectral shape of component 2. Then, a non-negative constraint is imposed. The results of the MCR-ALS analysis for the experimental data in the case of DMC-Li[BF_4] are shown in Figure 3.

SI 5. Normalization for Li[TFSI] solution

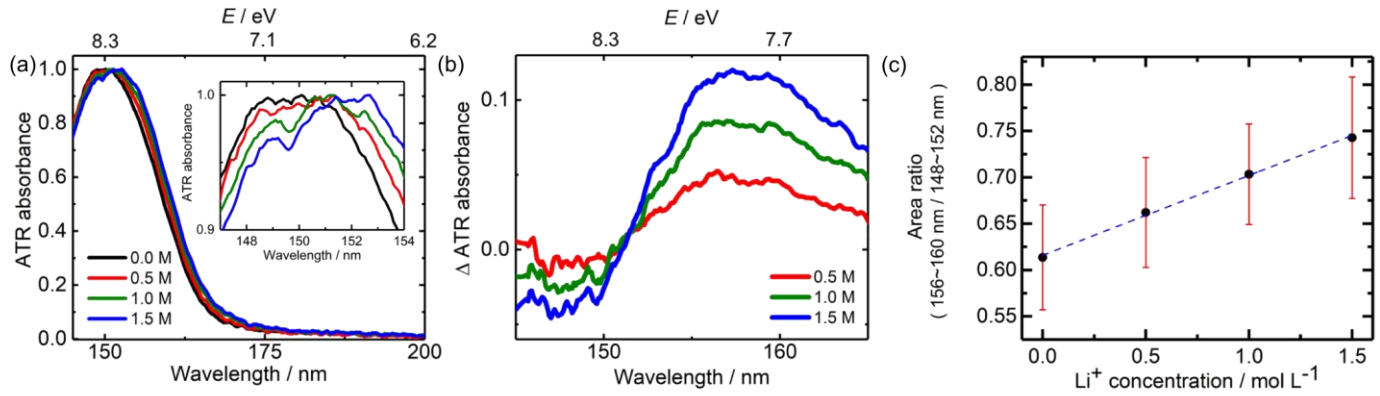

Figure S6 (a) Normalized spectra of pure DMC (black lines) and Li[TFSI] DMC solutions (colored lines) and (b) their difference spectra. (c) Li^+ concentration dependence of area ratio of the ATR spectral intensity in 156-160 nm to 148-152 nm in Figure 4(a). The standard deviation bar was calculated from the results of four ATR measurements.

The ATR spectra in Figure 4(a) were normalized to the maximum peak intensity (Figure S6(a)), showing that the peak wavelength slightly redshift with increasing Li^+ concentration. Figure S6(b) shows the normalized difference spectra, suggesting that the absorption at 158 nm can be attributed to Li^+DMC. Therefore, Li^+DMC has an absorbance at longer wavelengths (~158 nm) than free DMC (~150 nm). This redshift is more pronounced than that of $Li[BF_4]$ (Figure 1). The reason for this is discussed in SI 6. Figure S6(c) shows the Li^+ concentration dependence of area ratio of the ATR spectral intensity in 156-160 nm to 148-152 nm in Figure 4(a). As discussed above, the former absorbance (156-160 nm) is due to the Li^+DMC, and the latter (148-152 nm) was due to free DMC. As in the case of $Li[BF_4]$ DMC solutions, in the present concentration range (0.0-1.5 M), the area ratio was linearly related, indicating the uniform solvation structure.

SI 6. Effect of the counter anion ([TFSI]⁻) on the ATR spectrum

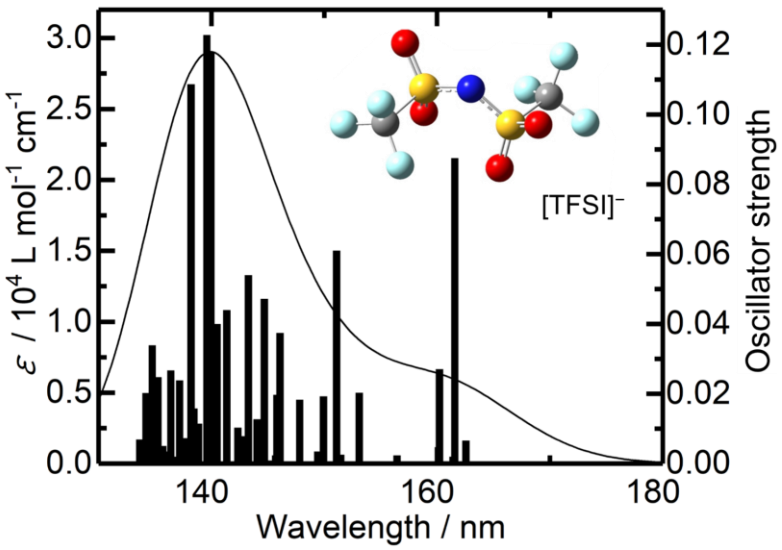

Figure S7 Time-dependent density functional theory (TD-DFT) calculated oscillator strengths and molar extinction coefficients (ε) of $[TFSI]^-$. This TD-DFT calculation was performed using the TD-CAM-B3LYP/aug-cc-pVTZ basis set. Based on the calculated vertical transition energies and oscillator intensities, the absorbance spectra were simulated assuming an energy width of 0.5 eV for each transition.

In the TD-DFT calculation of $[TFSI]^-$ (Figure S7), the oscillator strength and molar extinction coefficient (ε) are smaller than of DMC and Li^+DMC (Figure 2(a)), but not so small that it can be ignored. The ATR measurement range is 145-300 nm, and Figure S6 shows that $[TFSI]^-$ has absorption in this region. The details of main oscillator intensities are listed in Table S3.

Table S3 Calculated transition wavelengths, oscillator strength, main initial states, and main final states of $[TFSI]^-$.

Wavelength / nm	Oscillator strength	Initial state	Final state
161.6	0.0875	HOMO-1	LUMO+1
151.1	0.0610	HOMO	LUMO+13
144.8	0.0472	HOMO	LUMO+5
140.0	0.1179	HOMO-3	LUMO+4
139.6	0.1228	HOMO-2	LUMO+6

As mentioned earlier, we observed redshift of the peak wavelength with increasing Li^+ concentration, and this redshift are more pronounced for Li[TFSI] (Figure S6(b)) than for $Li[BF_4]$ (Figure 1(d)). This is thought to be due to the absorption peak of $[TFSI]^-$ around 160 nm.

Figure 4(a) and Figure S6(a) show the appearance of a small peak near 149 nm at 1.0 M and 1.5 M. This small peak is suggested to be derived from the oscillator intensity on the short wavelength side in Table S3. From the above, in the concentration range of Li[TFSI] in this study (0.0-1.5 M), the influence of the counter anion $[TFSI]^-$ is not large, but not so small as to be negligible. Therefore, the effect of $[TFSI]^-$ on the ATR spectrum should be considered.

SI 7. Multivariate analysis for DMC-Li[TFSI]

Figure S8(a) elucidates the decomposed absorption spectra obtained from the dataset inclusive of DMC-Li[TFSI], whereas (b) elucidates the contributions corresponding to the Li[TFSI] concentration added into DMC. The spectral shape of component 2 aligns with the MCR-ALS analyses for DMC-Li[BF_4]. Components 1 and 2 are as free-DMC and Li^+DMC, correspondingly, reflecting the MCR-ALS interpretations for DMC-Li[BF_4] as shown in Figure 3. Nonetheless, the peak center and absorbance of component 2 (DMC-Li[TFSI]) are longer and bigger compared to those of DMC-Li[BF_4]. The underlying cause for this redshift and enhanced absorbance is the encompassment of absorption related to $[TFSI]^-$ in component 2 of Figure S8, as previously mentioned in Figure S6 and S7. Thus, the increment in the contribution of component 2 (DMC-Li[TFSI]) with the increasing concentration of Li[TFSI] is notably more pronounced than that observed for DMC-Li[BF_4], by comparing Figures S8(b) and Figure 4(b).

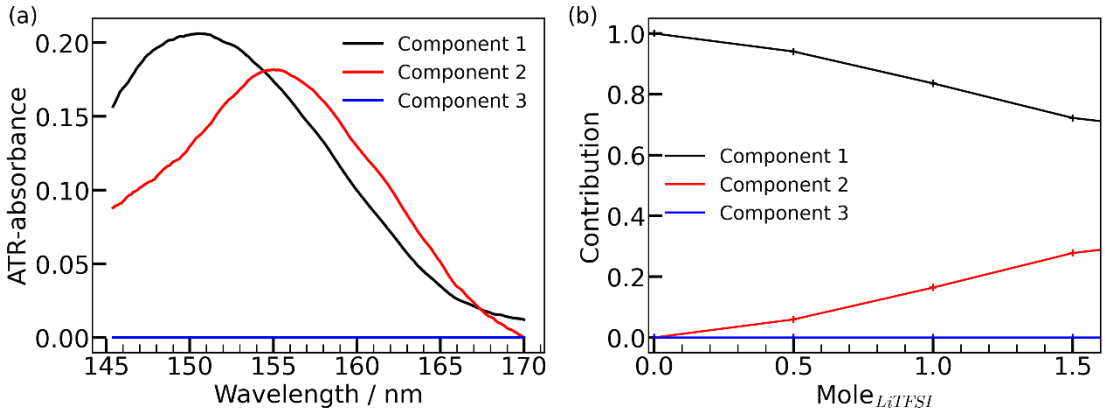

Figure S8(a) Decomposed absorption spectra ($S_{n,j}^T$) and (b) their contributions vs. Li^+ concentrations ($C_{i,n}$) analyzed using MCR-ALS calculations for i = 1, 2, and 3.

While the contributions of free DMC in 1.5 M for Li[BF_4] (Figure 3(b)) was 0.83, that for Li[TFSI] (Figure S8(b)) was 0.72. The contributions of Li^+DMC were 0.17 for Li[BF_4] (Figure 3(b)) and 0.28 for Li[TFSI] (Figure S8(b)), respectively. These results mean that more DMC molecules coordinated to Li^+ in Li[TFSI] solution than in Li[BF_4] solution. It should be noted here that the determining the specific values of the coordination number (CN) of DMC to Li^+ is still challenging. This is because the refractive index and density of the solutions changed depending on the Li^+ concentration. As a result, the number of DMC molecules detected in the ATR spectral measurements; i.e. the number of DMC molecules existing in the evanescent waves; varied with the Li^+ concentration. Additionally, as described above, the absorbance of $[TFSI]^-$ is small but not negligible. To determine the specific values of CN, it is necessary to consider these factors carefully. We are currently addressing this issue by utilizing not only ATR-FUV measurements and quantum chemical calculations but also molecular dynamics simulations and Raman spectroscopy.

SI 8. Details of Li[PF_6] solution in DMC solvent

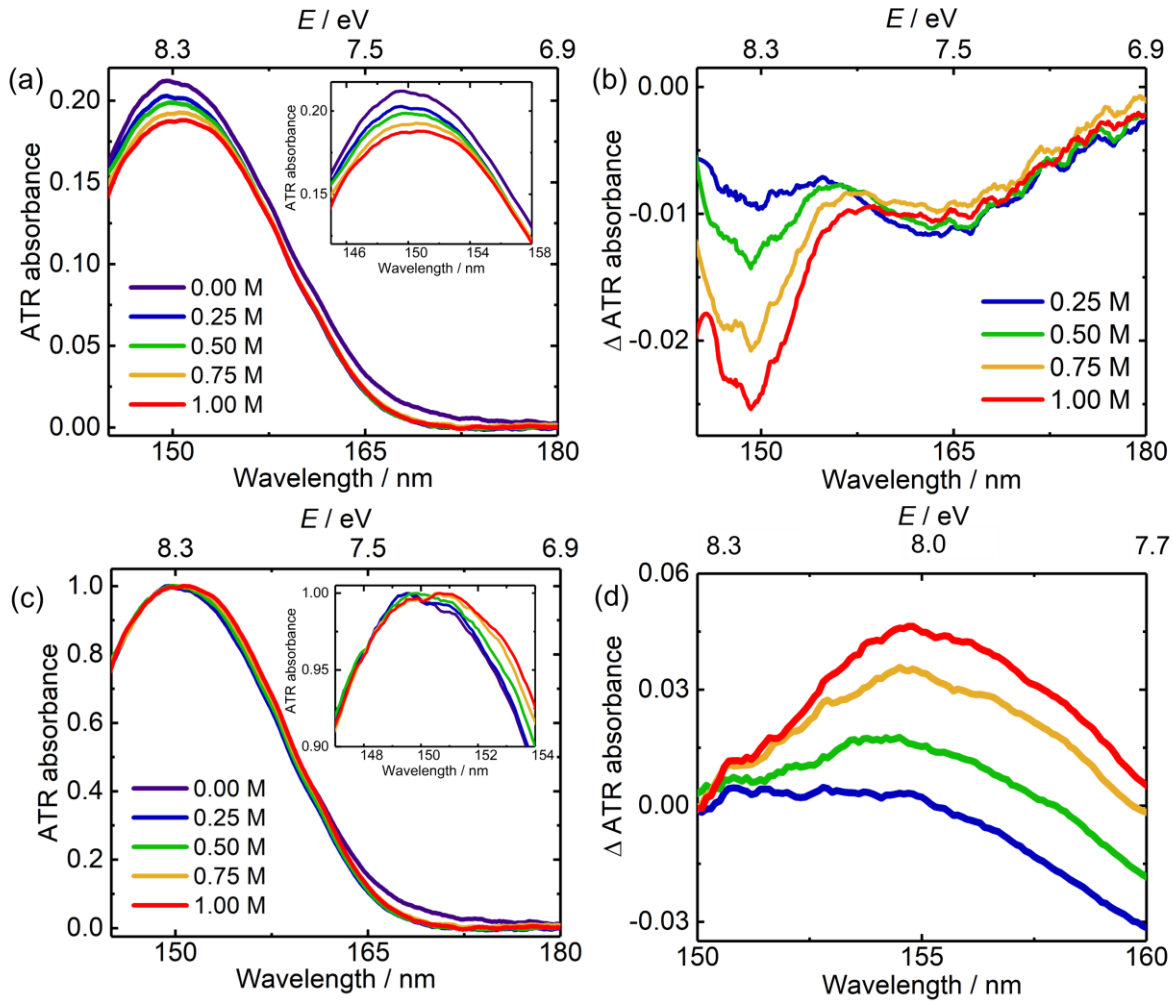

Figure S9 (a) ATR-FUV absorption spectra of pure DMC (purple line) and Li[PF_6] DMC solutions (other colored lines) at each Li^+ concentration in the 145−180 nm spectral region. (b) Difference spectrum from 0 M at each Li^+ concentration. (c) Normalized spectra of pure DMC (purple line) and Li[PF_6] DMC solutions (other colored lines) and (d) their difference spectra.

1.00 M Li[PF_6] solution (solvent: DMC) was purchased from Kanto Chemical Co., Inc. (Tokyo, Japan), and used without further purification. Li[PF_6] solutions of various concentrations (0.00, 0.25, 0.50, 0.75, and 1.00 M) were prepared. The measurement method is the same as for Li[BF_4] and Li[TFSI]. Note that this measurement wavelength range is limited to 145−180 nm because it focused on the DMC and Li^+DMC-derived peaks.

Figure S9(a) shows the ATR spectra of Li[PF_6] in DMC solvent in the 145−180 nm region. The difference spectra (Figure S9(b)) indicate decreases in spectral intensity around 150 nm with increasing Li^+ concentration. Figure S9(c) shows the normalized spectrum, which shows a slight redshift if the peak wavelength with increasing Li^+ concentration. Figure S9(d) shows the normalized difference spectra. By performing normalization based on the free DMC-derived peak around 150 nm and obtaining the difference spectra, the Li^+DMC-derived peak was observed. As a result, increases in peak intensity rear 155 nm was observed with increasing Li^+ concentration. As the Li^+ concentration increases, the amounts of Li^+DMC increases, suggesting that the absorption at 155 nm is attributed to Li^+DMC. Therefore, it can be concluded that Li^+DMC has an absorbance at longer wavelength (~155 nm) than free DMC (~150 nm).

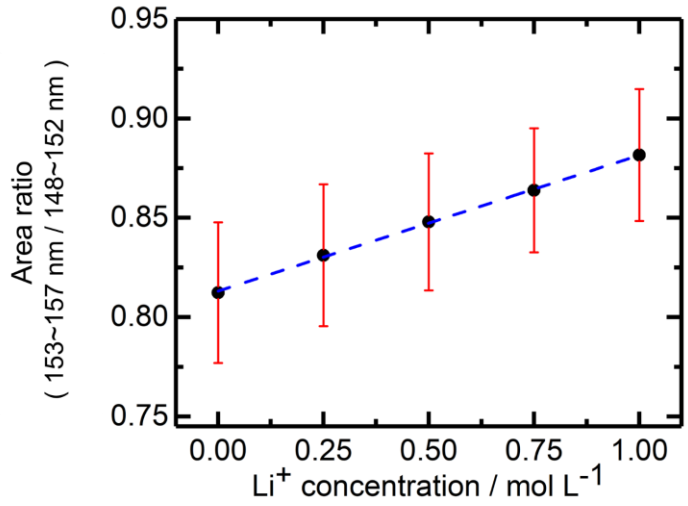

Figure S10 Li^+ concentration dependence of area ratio of the ATR spectral intensity in 153−157 nm to 148−152 nm in Figure S9(a). The standard deviation bar was calculated from the results of four ATR measurements.

Figure S10 shows the Li^+ concentration dependence of area ratio of the ATR spectral intensity in 153−157 nm to 148-152 nm in Figure S9(a). As discussed above, the former absorption (153−157 nm) is due to Li^+DMC, and the latter (148−152 nm) was due to free DMC. In the present concentration range (0.00−1.00 M), the area ratio was linearly related, indicating the uniform solvation structure.

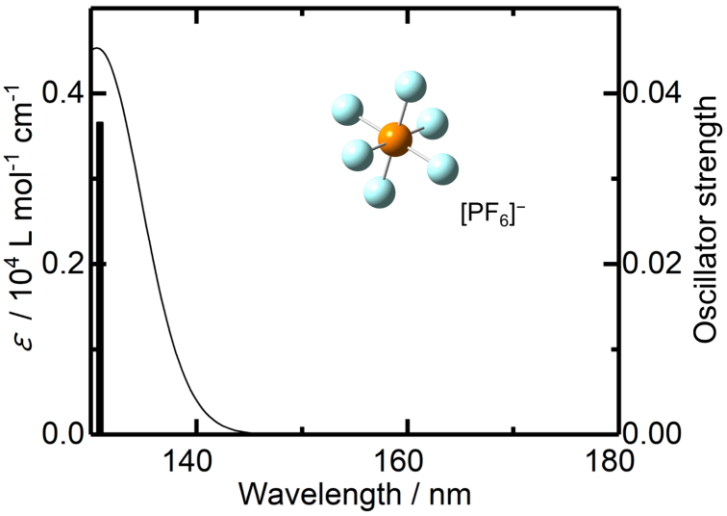

Figure S11 Time-dependent density functional theory (TD-DFT) calculated oscillator strength and extinction coefficients (ε) of $[PF_6]^-$. This TD-DFT calculation was performed using TD-CAM-B3LYP/aug-cc-pVTZ basis set. Based on the calculated vertical transition energies and oscillator intensities, the absorbance spectra were simulated assuming an energy width of 0.5 eV for each transition.

In the TD-DFT calculation of $[PF_6]^-$ (Figure S11), the oscillator intensity is not present in the wavelength region (145−180 nm) of the present study. The oscillator strength and molar extinction coefficient (ε) around 135 nm are also much smaller than DMC and Li^+DMC (Figure 2(a)). Additionally, the concentration of $Li[PF_6]$ is low (0.00−1.00 M). Therefore, it can be concluded that the effect of $[PF_6]^-$ is ignored in this study.